Supplemental Material for: Chiral Spin Mode on the Surface of a Topological Insulator

H.-H. Kung,[1,*] S. Maiti,[2] X. Wang,[1,3] S.-W. Cheong,[1,3] D. L. Maslov,[2,4,†] and G. Blumberg[1,5,‡]

[1] *Department of Physics & Astronomy, Rutgers University, Piscataway, New Jersey 08854, USA*
[2] *Department of Physics, University of Florida, Gainesville, Florida 32611, USA*
[3] *Rutgers Center for Emergent Materials, Rutgers University, Piscataway, New Jersey 08854, USA*
[4] *National High Magnetic Field Laboratory, Tallahassee, Florida 32310, USA*
[5] *National Institute of Chemical Physics and Biophysics, 12618 Tallinn, Estonia*

I. Material & Methods

Material preparation

The single crystals measured in this spectroscopic study were grown by modified Bridgman method. Mixtures of high-purity bismuth (99.999%) and selenium (99.999%) with the mole ratio Bi : Se = 2 : 3 were heated up to 870 °C in sealed vacuum quartz tubes for 10 hours, and then slowly cooled to 200 °C with rate 3 °C/h, followed by furnace cooling to room temperature.

The Bi_2Se_3 crystals used in this study were characterized by STM and phononic Raman scattering studies in Refs. [1, 2]. The Fermi energy (E_F) is determined by scanning tunneling spectroscopy to be about 150 meV above the Dirac point of SS1 [Fig. 1(b) in Main Text] [1]. Characterization confirmed that the samples have low concentration of impurities, Se vacancies, or other crystalline defects. All the bulk phonon modes in this crystal are sharp with no signatures of impurity modes, and all the expected surface phonon modes are clearly observed [2]. All spectroscopic features we present in this study were reproducible for a series of cleaves, immediately observed for each cool down, and did not show any signatures of time-dependent contamination.

Raman scattering

In this study, we used the 520.8, 647.1, 676.4 and 752.5 nm lines of a Kr^+ ion laser to promote secondary emission from the Bi_2Se_3 crystals. The spectra were acquired in a quasi-backscattering geometry from the ab surfaces, cleaved and transferred into the cryostat in nitrogen environment immediately prior to each cool down. About 10 mW of the laser power was focused into $50 \times 50\,\mu m^2$ laser spot. Scattered photons were collected and analyzed by a custom triple-grating spectrometer with a liquid nitrogen cooled charge-coupled device (CCD) detector. The secondary emission intensity, $\mathrm{I}_{\mu\nu}(\omega, T)$, was normalized to the laser power and corrected for the spectral response of the spectrometer and CCD, where μ (ν) is the polarization of incident (collected) photon. In a Raman process, $\mathrm{I}_{\mu\nu}(\omega, \mathrm{T})$ is related to the Raman response function, $\mathcal{R}_{\mu\nu}(\omega, T) = \mathrm{I}_{\mu\nu}(\omega, T)/[1 + n(\omega, T)]$, where $n(\omega, T)$ is the Bose-Einstein coefficient, ω is Raman shift and T is temperature.

The Raman response functions for given polarizations of incident and scattered photon are defined by the rank-2 Raman tensors, which can be symmetrized according to the irreducible representations of the crystal's point group. The scattering geometries used in this experiment are denoted as $\mu\nu$ =RR, RL, XX and XY, probing A_1+A_2, $2E_2$, A_1+E_2 and A_2+E_2 symmetries of the C_{6v} group, respectively [3, 4]. $\mathrm{R} = \mathrm{X} + i\mathrm{Y}$ and $\mathrm{L} = \mathrm{X} - i\mathrm{Y}$ denotes the right- and left-circular polarizations, respectively, where X (Y) denotes linear polarization parallel (perpendicular) to the plane of incidence.

After subtracting luminescence contributions (Sec. II), the measured spectra $\mathrm{I}_{\mu\nu}(\omega, \mathrm{T})$, are then decomposed into E_2, A_1 and A_2 symmetry channels as follows:

$$\begin{aligned}
\mathcal{R}_{E_2}(\omega, T) &= \frac{\mathrm{I}_{\mathrm{RL}}(\omega, T)}{2(1 + n(\omega, T))} \\
\mathcal{R}_{A_1}(\omega, T) &= \frac{\mathrm{I}_{\mathrm{XX}}(\omega, T) - \frac{1}{2}\mathrm{I}_{\mathrm{RL}}(\omega, T)}{1 + n(\omega, T)} \\
\mathcal{R}_{A_2}(\omega, T) &= \frac{\mathrm{I}_{\mathrm{XY}}(\omega, T) - \frac{1}{2}\mathrm{I}_{\mathrm{RL}}(\omega, T)}{1 + n(\omega, T)}.
\end{aligned} \tag{S1}$$

Computational details

In relation to Eq. (4) in the Main Text where we calculate the spin susceptibility, a momentum cutoff of $\Lambda_k = 0.3\,\text{Å}^{-1}$ was chosen. Any ambiguity that may arise due to the choice of cutoff can be subsumed into the interaction parameter U, thus making the physics of the appearance of the chiral spin collective modes universal. The threshold for the spin-flip continuum (ω_-) is obtained by finding the smallest ω such that $\Pi''(\omega, T = 0) \neq 0$. We find that $\omega_- \approx 260$ meV in the sample measured.

II. Photoluminescence contribution removal

Figure S1 shows the intensity of secondary emission measured for RR and RL polarizations at 24 K for 647, 676 and 752 nm excitation wavelengths, plotted as function of emission photon energy. The exciton emission centers at 1.54 eV for 647 and 676 nm excitations, and

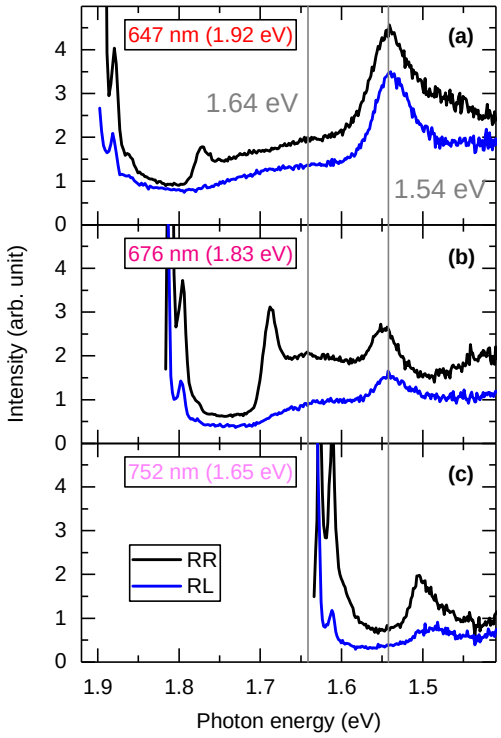

FIG. S1. Raman intensity measured in RR and RL polarizations at 24 K for (a) 647 nm (1.92 eV), (b) 676 nm (1.83 eV) and (c) 752 nm (1.65 eV) excitation energies, plot against scattered photon energy. The gray solid line marks 1.54 and 1.64 eV, where the exciton peaks centers coincide for 647 and 676 nm excitations, indicating that the peaks are due to photoluminescence emission rather than Raman scattering signal.

has about the same intensity for both RR and RL scattering geometries. Another weaker emission peak is observed at 1.64 eV for both excitations. These peaks are absent for 752 nm excitation spectra, suggesting that the emission has a threshold of about 1.8 eV.

To remove photoluminescence background from the measured spectra, we fit the 1.54 and 1.64 eV exciton peaks with a Lorentzian function, as shown by the hatched peaks in Fig. 2 of Main Text. We also subtract a small constant background from all spectra to account for other photoluminescence contribution.

III. Transitions between surface states and bulk bands

In this section, we present an explanation of spectroscopic features in Fig. 2(a) that are observed for a non-resonant excitation at 521 nm (2.38 eV).

Figure S2 shows the band structure of Bi_2Se_3 reconstructed from ARPES measurements [5]. The dispersion of the surface states is [6]:

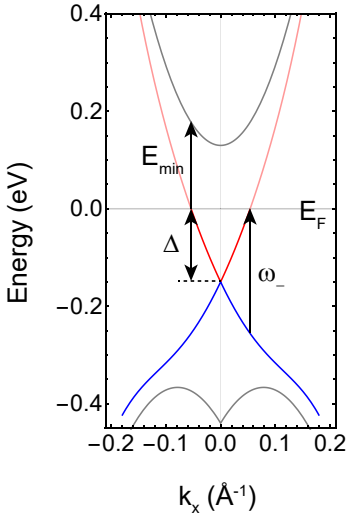

FIG. S2. Band structure near the Γ point and Fermi surface, reconstructed from ARPES measurements [5]. The blue and red lines denote the lower and upper Dirac cones, respectively, whereas the bulk bands are shown in gray. In the measured sample, the Dirac point is about 150 meV below the Fermi energy E_F.

$$E_{SS}(\mathbf{k}) = \Delta + \frac{k^2}{2m^*} \pm \sqrt{v_F^2 k^2 + \left(\frac{2v_3}{v_F}\right)^2 k^6 \cos^2 3\theta} \approx \Delta + \frac{k^2}{2m^*} \pm v_F k + 2\left(\frac{v_3^2}{v_F}\right) k^5 \cos^2(3\theta)\ , \quad \text{(S2)}$$

where $\pm$ denote the upper/ lower Dirac cones and θ is the azimuth angle of momentum $\mathbf{k}$ with respect to the x axis ($\Gamma - K$). Fitting the data in Ref. [5] to Eq. (S2) gives $m^* \approx 0.066\,\text{eV}^{-1}\text{Å}^{-2}$, $v_F \approx 2.4\,\text{eVÅ}$, and $v_3 \approx 25\,\text{eVÅ}^3$. One can readily see that the energy of a direct transition from the lower to upper Dirac cone is $2\sqrt{v_F^2 k^2 + (\frac{2v_3}{v_F})^2 k^6 \cos^2(3\theta)}$. In samples measured, Δ is determined by tunneling spectroscopy [1] to be about -150 meV, therefore the Fermi momentum $k_F \approx 0.054\,\text{Å}^{-1}$ along k_x, thus resulting in a threshold energy $\omega_- \approx 260$ meV.

The energy of a direct transition between SS1 and the bulk conduction band is given by $\epsilon(\mathbf{k}) = E_{CB}(\mathbf{k}) - E_{SS}(\mathbf{k})$, where $E_{SS}(\mathbf{k})$ is given by Eq. (S2), and the bulk conduction band dispersion follows a quasi-2D parabolic model [7]:

$$E_{CB}(\mathbf{k}) = E_0 + \frac{k_{||}^2}{2m_{||}^*} + \frac{k_\perp^2}{2m_\perp^*}, \quad \text{(S3)}$$

where $E_0 \approx 130$ meV is determined by E_F and the relative position between SS1 and bulk conduction band minimum [1, 5], $m_{||}^* \approx 0.03\,\text{eV}^{-1}\text{Å}^{-2}$ is the in-plane effective mass, determined from fitting the ARPES data in

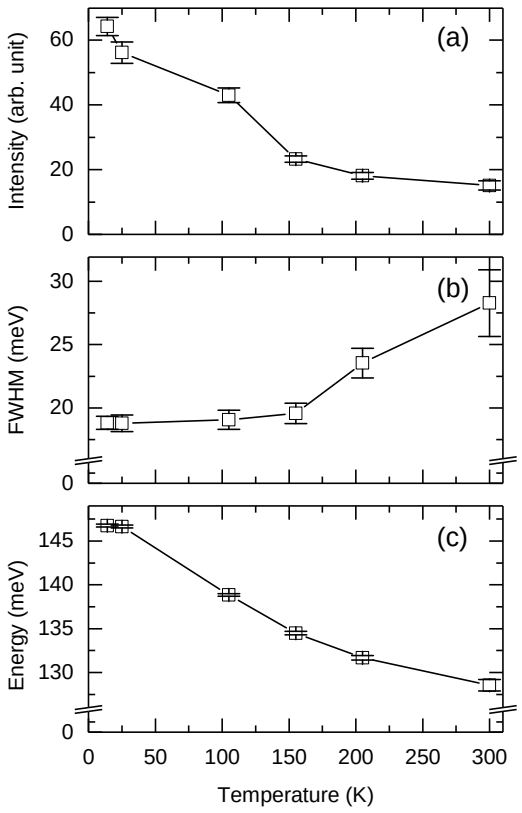

FIG. S3. Temperature dependence of (a) the intensity, (b) full width at half maximum (FWHM), and (c) peak center, of the chiral spin mode [Fig. 3(c) in the Main Text], fitted to a Lorentzian line shape. The error bars reflect one standard deviation of the fit.

Ref. [5] to quadratic dispersion. In the measured sample where $k_F \approx 0.054\,\text{Å}^{-1}$ along k_x, the threshold energy $E_{\min} \approx 180\,\text{meV}$, similar to what is seen in Fig. 2(a).

IV. Temperature dependence of the Raman peak from the surface chiral spin mode

Figure S3 shows the temperature dependence of the Raman intensity [(a)], full width at half maximum [FWHM, (b)], and peak center energy [(c)] of the chiral spin mode. The parameters were obtained by fitting the data in Fig. 3(c) of the Main Text to a Lorentzian lineshape. FWHM is approximately independent of temperature for $T \leq 150$ K. This indicates that the main damping mechanism of spin waves for these temperatures is due to disorder via the D'yanokov-Perel' mechanism [8]. This is in line with the theoretical predictions for damping of chiral spin waves [9, 10]. At higher temperatures, inelastic scattering mechanisms, e.g., electron-electron [10, 11] or electron-phonon [12] interactions, may also contribute to damping. However, we found that the model, which incorporates finite-temperature effects only via thermal smearing of the Fermi functions and neglects inelastic damping mechanisms, describes the experiment rather well. The results of this model with a T-independent damping rate of 8 meV (taken as 1/2 of FWHM at $T \to 0$) are shown in Fig. 3 (d) of the Main Text. On the other hand, the fact that the measured intensity decreases with increasing temperature faster than the calculated one may be an indication of unaccounted spin decay channels at elevated temperatures, e.g., through interaction with surface phonons [2].

* skung@physics.rutgers.edu
† maslov@phys.ufl.edu
‡ girsh@physics.rutgers.edu

[1] J. Dai, D. West, X. Wang, Y. Wang, D. Kwok, S.-W. Cheong, S. B. Zhang, and W. Wu, Phys. Rev. Lett. **117**, 106401 (2016).
[2] H.-H. Kung, M. Salehi, I. Boulares, A. F. Kemper, N. Koirala, M. Brahlek, P. Lošťák, C. Uher, R. Merlin, X. Wang, S.-W. Cheong, S. Oh, and G. Blumberg, Phys. Rev. B **95**, 245406 (2017).
[3] M. Cardona, in *Light scattering in solids II*, edited by M. Cardona and G. Güntherodt (Springer-Verlag, Berlin, 1982) pp. 45–49.
[4] L. N. Ovander, Opt. Spectrosc. **9**, 302 (1960).
[5] M. Nomura, S. Souma, A. Takayama, T. Sato, T. Takahashi, K. Eto, K. Segawa, and Y. Ando, Phys. Rev. B **89**, 045134 (2014).
[6] L. Fu, Phys. Rev. Lett. **103**, 266801 (2009).
[7] E. Lahoud, E. Maniv, M. S. Petrushevsky, M. Naamneh, A. Ribak, S. Wiedmann, L. Petaccia, Z. Salman, K. B. Chashka, Y. Dagan, and A. Kanigel, Phys. Rev. B **88**, 195107 (2013).
[8] M. I. D'yakonov and V. I. Perel', Sov. Phys. JETP **33**, 1053 (1971).
[9] A. Shekhter, M. Khodas, and A. M. Finkel'stein, Phys. Rev. B **71**, 165329 (2005).
[10] S. Maiti and D. L. Maslov, Phys. Rev. Lett. **114**, 156803 (2015).
[11] G. L. Bir, A. G. Aronov, and G. E. Pikus, Sov. Phys. JETP **42**, 705 (1975).
[12] D. L. Huber and J. H. Van Vleck, Rev. Mod. Phys. **38**, 187 (1966).